International Journal of Minerals, Metallurgy and Materials
Volume 29, Number 11, November 2022, Page 2020
https://doi.org/10.1007/s12613-021-2336-9

Effect of chromium interlayer thickness on interfacial thermal conductance across copper/diamond interface

Xiaoyan Liu[1)], *Fangyuan Sun*[2),✉], *Wei Wang*[3)], *Jie Zhao*[3)], *Luhua Wang*[1,4)], *Zhanxun Che*[5)], *Guangzhu Bai*[1)], *Xitao Wang*[6,7)], *Jinguo Wang*[4)], *Moon J. Kim*[4)], *and Hailong Zhang*[1),✉]

1) State Key Laboratory for Advanced Metals and Materials, University of Science and Technology Beijing, Beijing 100083, China
2) School of Energy and Environmental Engineering, University of Science and Technology Beijing, Beijing 100083, China
3) Beijing Institute of Structure and Environment Engineering, Beijing 100076, China
4) Department of Materials Science and Engineering, University of Texas at Dallas, Richardson, TX 75080, USA
5) Institute of Engineering Thermophysics, Chinese Academy of Sciences, Beijing 100190, China
6) Shandong Provincial Key Laboratory for High Strength Lightweight Metallic Materials, Advanced Materials Institute, Qilu University of Technology (Shandong Academy of Sciences), Jinan 250014, China
7) Collaborative Innovation Center of Steel Technology, University of Science and Technology Beijing, Beijing 100083, China
(Received: 17 April 2021; revised: 13 July 2021; accepted: 28 July 2021)

Abstract: The thermal conductivity of diamond particles reinforced copper matrix composite as an attractive thermal management material is significantly lowered by the non-wetting heterointerface. The paper investigates the heat transport behavior between a 200-nm Cu layer and a single-crystalline diamond substrate inserted by a chromium (Cr) interlayer having a series of thicknesses from 150 nm down to 5 nm. The purpose is to detect the impact of the modifying interlayer thickness on the interfacial thermal conductance (h) between Cu and diamond. The time-domain thermoreflectance measurements suggest that the introduction of Cr interlayer dramatically improves the h between Cu and diamond owing to the enhanced interfacial adhesion and bridged dissimilar phonon states between Cu and diamond. The h value exhibits a decreasing trend as the Cr interlayer becomes thicker because of the increase in thermal resistance of Cr interlayer. The high h values are observed for the Cr interlayer thicknesses below 21 nm since phononic transport channel dominates the thermal conduction in the ultrathin Cr layer. The findings provide a way to tune the thermal conduction across the metal/nonmetal heterogeneous interface, which plays a pivotal role in designing materials and devices for thermal management applications.

Keywords: sputtering; diamond; metal/nonmetal interface; interfacial thermal conductance; time-domain thermoreflectance

1. Introduction

As the characteristic dimension of electronic components is scaling down at a speed of Moore's law, the micro-nanometer manufacturing techniques have advanced to the node of 7 nm [1–5]. However, as the surface area of the electronic components varies inversely with the square of their characteristic scale, the heat flow density increases dramatically during operation, leading to heat concentration and temperature exorbitance. If the high heat flux is not dissipated in a short time, it may cause the degradation in performance and reliability of the electronic devices [5–6]. With the improvement of integration and packaging density, heat dissipation becomes a critical issue for the electronic packaging design.

Diamond particles reinforced copper matrix (Cu/diamond) composites have become a fresh region of metal matrix composites [7] for heat dissipating and spreading in electronic encapsulation because of the excellent thermal conductivity (λ) and proper coefficient of thermal expansion (CTE). As the Cu matrix is inert to the diamond reinforcement, weak interfacial bonding is observed in the composites. To resolve this issue, researchers have added carbides such as Cr_3C_2 [8–11], TiC [12–15], ZrC [16–17], Mo_2C [18–19], WC [20], and B_4C [21] at Cu/diamond interface through diamond surface metallization or metal matrix alloying to enhance the interfacial adhesion and bridge the phonon spectra mismatch between Cu and diamond [22–23]. Our previous work presented the influence of Cr modification on the thermal conductivity of Cu/diamond composites and reported a high thermal conductivity of 810 $W \cdot m^{-1} \cdot K^{-1}$ for Cr-modified Cu/diamond composites [24].

The interfacial thermal conductance (h) is critical to heat transfer in the Cu/diamond composites. Blank and Weber [25] demonstrated the impact of dielectric surface termination (HF-dipped or radio frequency (RF)-etched) on the heat transfer across a great variety of metal/Si interfaces, and suggested that the interfacial bonding is crucial to controlling the heat transfer across these interfaces. When the interfacial

✉ Corresponding authors: Fangyuan Sun E-mail: sunfangyuan@ustb.edu.cn; Hailong Zhang E-mail: hlzhang@ustb.edu.cn
© University of Science and Technology Beijing 2022

bonding strength is lower than 100 $mJ \cdot m^{-2}$, the interfacial bonding is the predominant factor of heat transfer of the interface. When the interfacial adhesive strength is above 100 $mJ \cdot m^{-2}$, however, the predominant factor becomes the vibrational mismatch of phonons of the two materials on both sides of the interface [12,26]. The Cr modification could enhance the interfacial adhesion between the diamond reinforcement and the Cu matrix. Nevertheless, the details about h of the Cu–Cr/Cr–diamond composites are not released, and the effect of Cr modification on interfacial thermal conductance is also not clarified. It is worthy to note that for some carbide-forming elements such as VIB group metals Cr, Mo, and W, the thermal conductivity of the carbide is much lower than the metal. The conversion of the metals into carbides could decrease the h value between Cu and diamond. Both experimental and theoretical studies have shown that the h value of the Cu/Cr_3C_2/diamond structure is lower than that of the Cu/Cr/diamond structure [11]. The modification of Cu/diamond interface using the metallic interlayer could be a better choice. Jeong *et al*. [23] and Blank and Weber [27] have researched the effect of the metallic interlayer thickness on the h across Au/metal/sapphire, Au/metal/silicon, and Au/metal/diamond interfaces. To date, the impact of the metallic interlayer thickness on the interfacial thermal conductance between Cu and diamond has not been reported. For instance, Cr has an electronic mean free path of 15.2 nm [28]. The selection of the Cr interlayer thickness with respect to the feature value could greatly affect the interfacial thermal conductance between Cu and diamond. The purpose of this article is to detect the effect on the h value of the Cu/diamond interface by tuning the Cr interlayer thickness in Cu/Cr/diamond samples. The metal Cr is selected as the interlayer for other two reasons: (1) since Cr has a high affinity for carbon, the Cr interlayer improves adhesion between Cu and diamond [29–30]; (2) since the Debye temperature of Cr is in between Cu and diamond, the Cr interlayer improves bridging [31].

Heat conduction across the heterogeneous interface in the Cu/diamond composite needs to be fully understood to control the efficient heat dissipation better. Heat conduction mechanisms across the heterogeneous interface builds up the basis of theoretical and experimental studies. For a metal/nonmetal heterogeneous interface, complicated pathways of heat transport are involved, such as the electron or phonon transmission across the interface, the electron–phonon interaction in the metal or at the interface [23,32–34]. The electron–phonon coupling is critical in the thermal energy conversion between Cu and diamond because phonons are the dominant heat carriers in diamond, while electrons are the dominant heat carriers in Cu. The view is widely shared that the dominant heat transport channel in Cu/diamond composite is phononic conduction, and therefore the electronic thermal conduction pathways are usually neglected in most of the researches on the interfacial thermal conductance of Cu/diamond composite. In this paper, three interfacial thermal conduction pathways are considered for the Cu/Cr/diamond nanostructure, including phonon transmission ($R_{pp} = 1/h_{pp}$, where R_{pp} and h_{pp} are the phononic interfacial thermal resistance and conductance, respectively), electron transmission ($R_{ee} = 1/h_{ee}$, where R_{ee} and h_{ee} are the electronic interfacial thermal resistance and conductance, respectively), and electron–phonon coupling in the metal film near the interface ($R_{ep} = 1/h_{ep}$, where R_{ep} and h_{ep} are the resistance and conductance to heat transfer between electron and phonon in the metal just before the heat flows into/from phonons on the other side, respectively). The phononic thermal conduction pathway can be theoretically predicted by various methods, for example, molecular dynamics (MD) simulations [35–37], acoustic mismatch model (AMM) [10,13,16,21], diffusive mismatch model (DMM) [11–12,38], and nonequilibrium Green's function (NGF) method [39]. The DMM is used to describe the phononic thermal conduction pathway across the interface. Gundrum *et al*. [40] have developed the DMM from phonon to electron to deal with the thermal conduction pathway of electron transmission [27,32,40–41]. The thermal conduction pathway of electron–phonon coupling can be theoretically predicted by a diffusive two-temperature model (TTM), which has been generally applied to interpret pump–probe experiment observations [33–34,42–46]. The TTM is used to model the metal/nonmetal interface considering the diffusive electronic thermal conduction in the metal film near the interface.

In this article, we insert a nanometer-thick Cr thin film at the Cu/diamond interface by magnetron sputtering and tune the thickness of the Cr interlayer by varying the sputtering time of the Cr layer. The h values of the Cu/diamond interfaces are directly measured via an experiment system of time-domain thermoreflectance (TDTR). The measurement shows that the h value firstly increases by inserting a 5 nm-thick Cr interlayer and then decreases continually as the Cr interlayer thickness increases to 150 nm. We demonstrate that the electronic thermal transport channel could not be ignored when the Cr interlayer thickness is less than the electron mean free path. The results suggest that regulating an appropriate interlayer thickness helps enhance the interfacial thermal conductance of Cu/diamond interface.

2. Experiment and calculation

2.1. Sample preparation

The Cr film and Cu film were prepared on a synthetic monocrystalline diamond substrate (HSCD11, Huanghe Whirlwind Co., China) in an argon atmosphere at room temperature via the direct current (DC) magnetron sputtering (Discovery 635, DENTON, USA). The [100]-oriented diamond plates have a size of around 2.5 mm × 2.5 mm × 1 mm. The λ of the diamond plates was calculated to be 1647 $W \cdot m^{-1} \cdot K^{-1}$ based on the nitrogen content (169 ppm, type Ib). The target materials for sputtering Cr and Cu nanometer films both have purities higher than 99.999%. Cr films with thicknesses in the range of 5–150 nm were firstly deposited on the diamond plates, and a thin Cu film with a thickness of

200 nm was then deposited on the Cr film. A schematic of the samples is shown in Fig. 1.

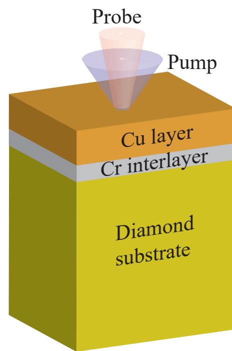

Fig. 1. Schematic diagram of Cu/Cr/diamond setup for TDTR measurement.

The root mean square (RMS) roughness values of the diamond substrate surfaces were controlled to be ~1 nm through a succession of mechanical polishing with 10 μm, 5 μm, and 2.5 μm diamond suspensions. The diamond substrates were ultrasonically cleaned in acetone, ethanol, and isopropanol baths, followed by treatment in a gas composition of Ar : O_2 = 3:1 (volume ratio) for 15 min using a Fischione 1020 oxygen plasma cleaner. The operations serve to clear up the surface impurities and organic contaminants during mechanical polishing.

The distance between diamond substrates and the targets was set to 150 mm in the sputtering machine. Before depositing the metal bilayer, the substrates were treated by a bombardment of ion beam cleaning for 10 min under a pressure of 0.6 Pa to eliminate adsorbed impurities and native oxides. It is noted that the bombardment time cannot be too long; otherwise, the disorder of carbon atoms could be induced on the diamond substrate surface [47]. We have checked the bombardment-cleaned diamond surface and do not find disordered carbon atoms on the diamond surface [11]. The base vacuum pressure of <5.3 × 10^{-5} Pa and sputtering power of 300 W were used for all the samples. The working pressures for sputtering Cr and Cu films were 0.80 and 0.48 Pa, respectively. The deposition rates for Cr and Cu were 0.24 and 0.38 nm·s^{-1}, respectively. The surface profiler (KLA-Tencor P-6, USA) was used to determine the film thickness. The thickness of each layer was further confirmed by transmission electron microscope (TEM). The obtained Cu/Cr/diamond nanostructure samples were used for subsequent TDTR measurements.

2.2. Material characterization

Atomic force microscope (AFM, Dimension FastScan, Germany) was used to measure the surface roughness of the diamond substrates. X-ray diffraction (XRD, Rigaku DMAX-RB, Japan) was implemented to characterize the phase composition of the Cu/Cr films. Auger electron spectrometer (AES, PHI 700, Japan) was employed to provide the chemical state and depth profile information across the interface, including composition, concentration, and intensity of elements [48–49]. The microstructure and phase composition were examined by TEM (JEOL 2100F, Japan) and scanning transmission electron microscope (STEM, JEOL ARM200, Japan). The TEM specimens were fabricated using a dual-beam focused ion beam station (FIB, FEI Nova 200, USA).

2.3. Thermal characterization

We employ the TDTR method to investigate the interfacial thermal conductance between Cu and diamond with an inserted Cr film having various thicknesses. The femtosecond laser pump-and-probe setup has been described in detail elsewhere [9]. In brief, the output of a mode-locked Ti:sapphire laser with a wavelength of 800 nm is separated into two routes. The pump laser is focused on the film surface to heat it. The slight changes in the optical reflectivity of the sample surface are measured by the probe laser [50–54]. The pulse width and repetition rate of the Ti:sapphire laser are 100 fs and 80 MHz, respectively. The modulation frequency of the pump laser is fixed at 1 MHz using an electro-optic modulator. The spot size of the pump beam is 80 μm. All the tests were performed at ambient temperature. The experimental data were fit to a thermal model to extract the thermal properties of interest.

2.4. Theoretical prediction of interfacial thermal conductance

The theoretical model is applied to predict interfacial thermal conductance and provides insights into the physical mechanisms. The interfacial thermal conductance between two different materials is estimated based on the Debye model [55–59]:

$$h = \frac{1}{4}\rho_{\text{in}} c_{\text{in}} v_{\text{in}} \eta \tag{1}$$

where the ρ, c, v, and η are the mass density, specific heat capacity, Debye (or effective) sound velocity, and average probability for the phonon transmission across an interface, respectively. The subscript “in” denotes the material in which the phonon is incident. For the DMM, the interfacial thermal conductance is further presented by [58–60]:

$$h = \frac{1}{4}\frac{\rho_{\text{in}} c_{\text{in}} v_{\text{in}}^3}{v_{\text{in}}^2 + v_{\text{tran}}^2} \tag{2}$$

where the subscript “tran” denotes the material in which the phonon is transmitted. The phononic interfacial thermal resistance R_{pp} can be formulated by $R_{\text{pp}} = 1/h$. The required material parameters for the calculation of R_{pp} are summarized in Table 1 [9,11,34,55,61–62]. The total h between Cu and diamond for the Cu/Cr/diamond sample is given by:

$$\frac{1}{h} = \frac{1}{h_{\text{Cu/Cr}}} + \frac{l_{\text{Cr}}}{\lambda_{\text{Cr}}} + \frac{1}{h_{\text{Cr/diamond}}} \tag{3}$$

where l_{Cr} is the Cr interlayer thickness.

The deficiency is that the DMM model only takes the phononic thermal conduction pathway into account. Unfortunately, the predictive value is relatively low in most instances as the electronic thermal conduction pathway on the

Table 1. Material parameters for calculations of *h* using DMM

Material	ρ / (kg·m^{-3})	λ / (W·m^{-1}·K^{-1})	c / (J·kg^{-1}·K^{-1})	v / (m·s^{-1})
Cu	8900 [61]	401 [34]	386 [61]	2881 [11,61–62]
Cr	7190 [61–62]	90 [61]	446 [61]	4637 [9,61–62]
Diamond	3512 [55,62]	1647 [11]	512 [61]	12775 [11]

metal side is neglected. Previous studies show that the diffusive two-temperature model (TTM) is convenient to estimate electron–phonon coupling within the metal layer near the interface [34,42,44,63–64]. The TTM splits electron and phonon into two separate subsystems and gives the temporal and spatial evolution of their temperatures, which is designed to qualitatively evaluate the contribution of electrons on the metal side. The steady-state TTM describes the energy balance in the metal and is given by [34,42,44,63–64]:

$$\lambda_{\mathrm{e}}\frac{\partial^2 T_{\mathrm{e}}}{\partial x^2} - G\left(T_{\mathrm{e}} - T_{\mathrm{p}}\right) = 0 \tag{4}$$

$$\lambda_{\mathrm{p}}\frac{\partial^2 T_{\mathrm{p}}}{\partial x^2} + G\left(T_{\mathrm{e}} - T_{\mathrm{p}}\right) = 0 \tag{5}$$

where λ and T are the thermal conductivity and temperature of electrons or phonons (subscript e or p), and G is the electron–phonon coupling factor concerning the rate of energy exchange from electron to phonon [45]. Metals have typical G on the order of 10^{16}–10^{17} W·m^{-3}·K^{-1} [42,65]. For steady-state heat flow across a film, combining Eqs. (4) and (5) with the Fourier's law yields [34,42,44,63–64]:

$$-J = \lambda_{\mathrm{e}}\nabla T_{\mathrm{e}} + \lambda_{\mathrm{p}}\nabla T_{\mathrm{p}} \tag{6}$$

where J is the heat flux. Then, the total interfacial thermal resistance of the two-segment system is thus obtained [34,42,44,63–64]:

$$R = \frac{\Delta T}{J} = R_{\mathrm{pp}} + R_{\mathrm{ep}} = \frac{1}{h_{\mathrm{pp}}} + \left(\frac{\lambda_{\mathrm{e}}}{\lambda_{\mathrm{e}} + \lambda_{\mathrm{p}}}\right)^{\frac{3}{2}}\left(\frac{1}{G_{\mathrm{ep}}\lambda_{\mathrm{p}}}\right)^{\frac{1}{2}} \tag{7}$$

where G_{ep} is the electron–phonon coupling factor in the metal just before the heat flows into/from phonons on the other side.

Finally, a simplified form for R_{ep} within the metal layer near the interface is defined [34,42,44,63–64]:

$$R_{\mathrm{ep}} = \left(\frac{\lambda_{\mathrm{e}}}{\lambda_{\mathrm{e}} + \lambda_{\mathrm{p}}}\right)^{\frac{3}{2}}\left(\frac{1}{G_{\mathrm{ep}}\lambda_{\mathrm{p}}}\right)^{\frac{1}{2}} \tag{8}$$

Gundrum *et al.* [40] have developed the DMM from phonon to electron, and the metal–metal electronic interfacial thermal resistance R_{ee} is estimated [33,40–41]:

$$R_{\mathrm{ee}} = \frac{4(Z_1 + Z_2)}{Z_1 Z_2} \tag{9}$$

where $Z_1 = C_{\mathrm{e1}}v_{\mathrm{F1}}$ and $Z_2 = C_{\mathrm{e2}}v_{\mathrm{F2}}$, and the volumetric heat capacity of the electron C_{e} is calculated as $C_{\mathrm{e}} = \gamma T_{\mathrm{e}}$, with electron specific heat constant γ (Sommerfeld's constant) and Fermi velocity v_{F} [40,44,66–71]. The required material parameters for the calculations of R_{ep} and R_{ee} are summarized in Table 2 [31,37,64–65,67,69,72–77].

Table 2. Physical constants for calculations of *R*

Material	λ_{e} / (W·m^{-1}·K^{-1})	λ_{p} / (W·m^{-1}·K^{-1})	G_{ep} / (10^{16} W·m^{-3}·K^{-1})	γ / (J·m^{-3}·K^{-2})	v_{F} / 10^6 (m·s^{-1})	σ / (10^8 Ω^{-1}·m^{-1})	L / (10^{-8} W·Ω·K^{-2})	c_{p} / (10^6 J·m^{-3}·K^{-1})
Cu	384 [37]	17 [37]	26 [31]	96.6 [72–73]	11.09 [75]	—	—	3.5 [72]
Cr	57.096[a]	32.904[b]	42 [64]	194 [67,69,74]	0.246 [76]	0.078 [77]	2.44 [76]	3.24 [65]

Note: [a] Calculated by $\lambda_{\mathrm{e}} = LT\sigma$; [b] Calculated by $\lambda_{\mathrm{p}} = \lambda - \lambda_{\mathrm{e}}$.

The three-segment system is composed of metal A/metal B/nonmetal C, as shown in Fig. 2. The coexistence of electronic and phononic thermal conduction pathways, however, makes the thermal conduction behave in a relatively complicated manner.

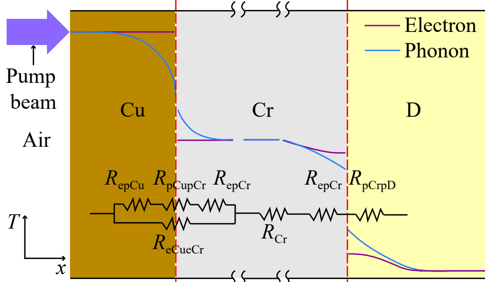

Fig. 2. Thermal conduction mechanisms at Cu/diamond interface with Cr interlayer. The red and blue solid lines represent the electronic and phononic thermal conduction pathways, respectively. D is diamond, *T* is temperature, and *x* is distance.

We struggle to interpret all kinds of thermal conduction pathways and evaluate the impact of interlayer on interfacial thermal conductance in the Cu/Cr/diamond system. For the combined DMM and TTM models, the interfacial thermal conduction pathways include phonon–phonon coupling, electron–electron coupling, and electron–phonon coupling in the metal near the interface. In this way, the prediction can be closer to realistic thermal conduction events in heterojunctions with the metal/nonmetal interface. Based on the above analysis, we draw a simple diagram to describe the thermal conduction mechanisms at Cu/diamond interface with a Cr interlayer, as shown in Fig. 2. We therefore obtain the interfacial thermal resistance between Cu and Cr as $R_{\mathrm{iepCu/Cr}} = 1/\left(\frac{1}{R_{\mathrm{epCu}} + R_{\mathrm{pCupCr}} + R_{\mathrm{epCr}}} + \frac{1}{R_{\mathrm{eCueCr}}}\right)$, where R_{epCu} is the res-

istance to heat transfer between electron and phonon in the Cu layer just before the heat flows into/from phonons on the other side, R_{pCupCr} is the phononic interfacial thermal resistance between Cu and Cr, R_{epCr} is the resistance to heat transfer between electron and phonon in the Cr interlayer just before the heat flows into/from phonons on the other side, and R_{eCueCr} is the electronic interfacial thermal resistance between Cu and Cr. Then, the overall interfacial thermal resistance between Cu and diamond is written as:

$$R = R_{iepCu/Cr} + R_{Cr} + R_{epCr} + R_{pCrpD} \tag{10}$$

3. Results and discussion

3.1. Surface morphology and interface structure of Cu/Cr/diamond samples

The microstructural evolution of the Cu/Cr/diamond samples was investigated by scanning electron microscope (SEM) and AFM. The SEM image of the top surface of the Cu layer is shown in Fig. 3(a). After magnetron sputtering, uniform and spherical Cu particles were obtained. To determine the surface roughness, AFM was employed to scan the top surface of the Cu layer. The 3D surface morphology of the Cu/Cr/diamond sample is shown in Fig. 3(b). The line profile in Fig. 3(c) shows that the depth of surface steps varies from about +5 nm to −5 nm. The RMS roughness of the Cu surface is around 2.56 nm. To minimize TDTR test errors, the surface roughness of the samples should be less than 15 nm [78]. All the sample surfaces are smooth enough to satisfy the TDTR test requirements.

The phase structure was characterized by XRD, as represented in Fig. 4. For the Cu film on diamond substrate, only Cu (111), (200), and (220) peaks are observed at 43.3°, 50.5°, and 74.2°, respectively. Besides Cu peaks, Cr (110) peak is also observed at 44.4° for the Cu/Cr bilayer film on diamond substrate.

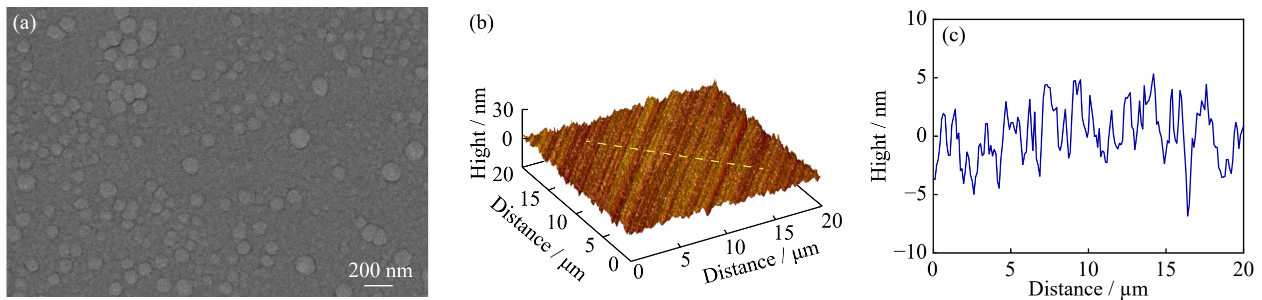

Fig. 3. Surface morphology of the top Cu film: (a) SEM image; (b) AFM image; (c) surface roughness measurement along the dashed line in (b).

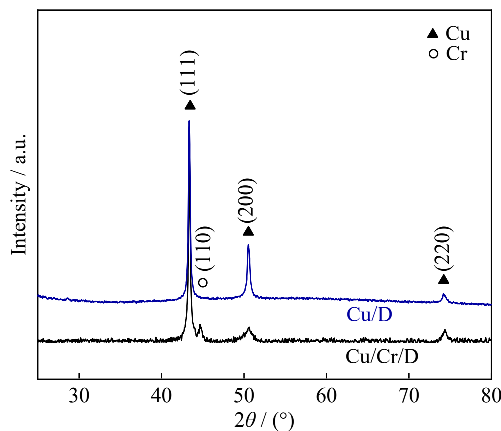

Fig. 4. XRD patterns of the Cu/diamond and Cu/Cr/diamond samples.

The depth profile and chemical state for the Cu/diamond and Cu/Cr/diamond samples were measured by AES, as shown in Figs. 5 and 6. In Fig. 5(b) or Fig. 6(b), Cu LMM spectrum for pure Cu consists of one kinetic energy peak at 919 eV [79]. As the depth is increased, the kinetic energies and line shapes remain unchanged. It can be concluded that metallic Cu exists in the Cu layer. A similar result is obtained from Cr LMM spectrum in Fig. 6(c). At depths C and D, the kinetic energies of Cr LMM are 528 eV, consistent with pure Cr [80]. It is confirmed that metallic Cr exists at the Cu/diamond interface. The line shapes of C KLL at depths C and D in Figs. 5(c) and 6(d) show one characteristic peak at 267 eV, consistent with diamond [14,79,81]. It indicates that C exists as diamond. The oxygen adsorption in the Cu/Cr bilayer film is also detected; however, the concentration of oxygen in the metal layers is very low. Interface diffusion takes place at Cr/diamond interface and sometimes Cr_3C_2 is formed during deposition of Cr layer at room temperature, as reported in references [82–83]. The bombarding energy of Cr atoms during sputtering deposition results in the interface diffusion and chemical reaction [83]. Nevertheless, we did not observe the formation of Cr_3C_2 in this article.

The h of Cu/diamond is greatly affected by the interfacial structure and interfacial adhesion between the Cu layer and the diamond substrate [78]. Further study by TEM gives more information about the microstructure at the Cu/diamond interface. Fig. 7(a) presents the cross-sectional view of the Cu/Cr/diamond sandwich structure. The columnar grains in the Cu layer and the ultrafine nanocrystals in the Cr interlayer are observed. The thicknesses of the Cu layer and Cr interlayer are estimated at around 200 and 100 nm, respectively. The HRTEM images in Fig. 7(b) and (c) display the Cu/Cr and Cr/diamond interfaces, respectively. Cu (200) plane is prepared on Cr (110) plane, and Cr (110) plane is de-

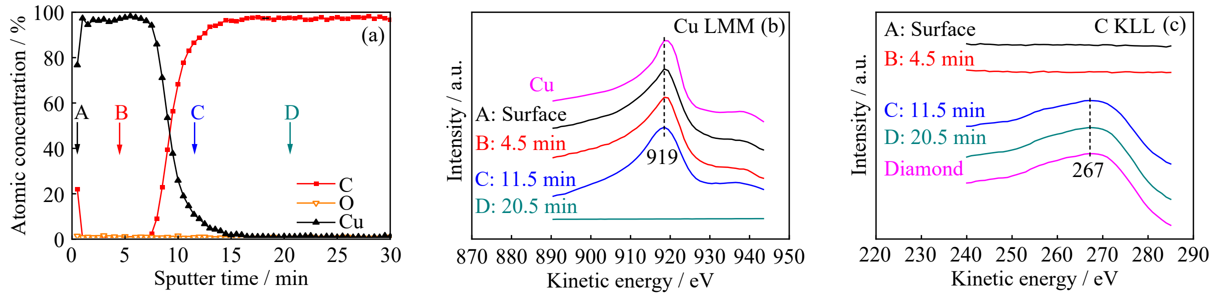

Fig. 5. (a) AES depth profile spectra for the Cu/diamond and the corresponding Auger kinetic energy spectra of (b) Cu LMM and (c) C KLL.

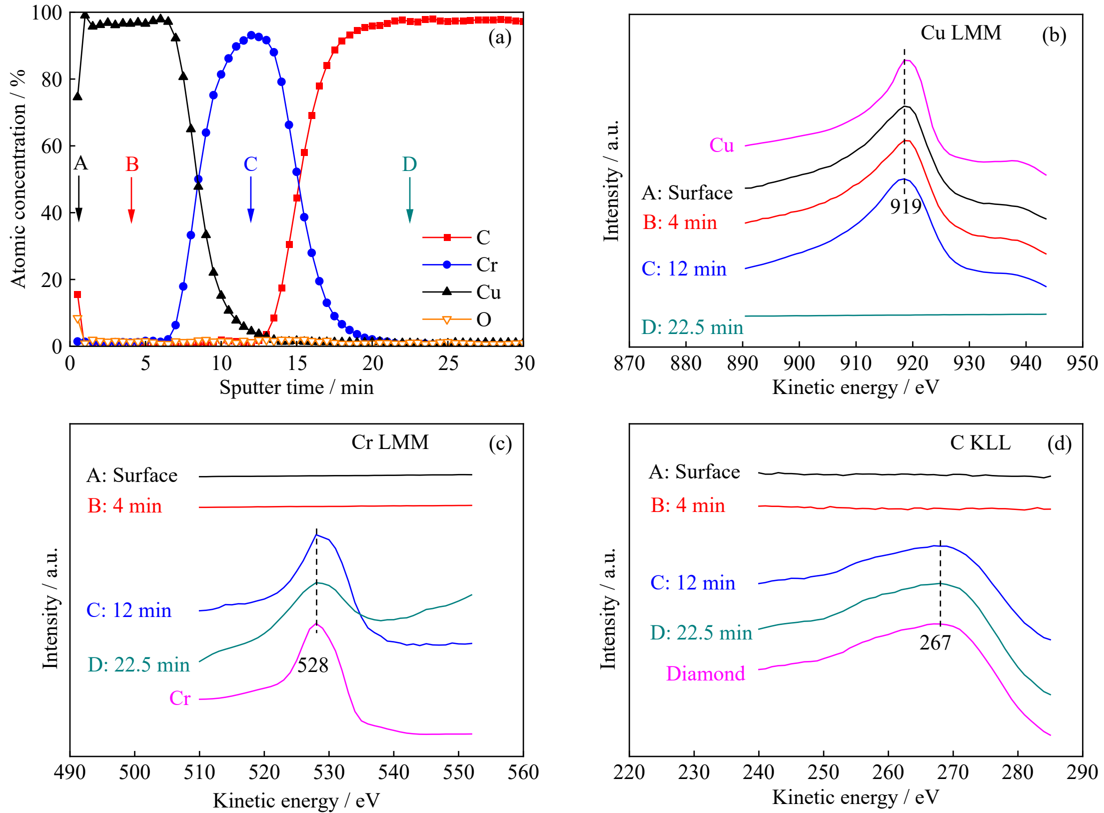

Fig. 6. (a) AES depth profile spectra for the Cu/Cr/diamond with 100 nm Cr and the corresponding Auger kinetic energy spectra of (b) Cu LMM, (c) Cr LMM, and (d) C KLL.

posited on diamond (220) substrate. The HRTEM images of the Cu film in Fig. 7(b) and (d) show that Cu (111) and (200) planes have interplanar spacings of 0.209 and 0.181 nm, which are analogous to the standard values of $d_{(111)}$ = 0.2086 nm and $d_{(200)}$ = 0.1806 nm (PDF#70-3039), respectively. As shown in Fig. 7(e), Cr (110) plane is measured with an interplanar spacing of 0.204 nm, which is aligned with the reference value of $d_{(110)}$ = 0.2039 nm (PDF#06-0694). The TEM results are in good agreement with the XRD patterns in Fig. 4. Since the Cr film is sputtered at room temperature, no carbide is observed at the Cr/diamond interface [11].

In order to investigate the crystallite size distribution of the Cr interlayer, the Cr film was observed by SEM before sputtering Cu film. Fig. 8(a) shows that polycrystalline Cr film grows on diamond substrate, and the oval-shaped grains are observed. The length distribution of the Cr grains was obtained using an average diameter analysis software (Nano Measurer). For the 100 nm-thick Cr film, the length of the oval-shaped Cr grains is in the range of 40–65 nm, as shown in Fig. 8(b).

3.2. Interfacial thermal conductance between Cu and diamond

The *h* values of the Cu/diamond and Cu/Cr/diamond samples were measured by TDTR at ambient temperature (around 26°C). The measurement sensitivities of the amplitude signal fittings for the samples are shown in Fig. 9. The best fitting curves, as well as the simulated lines with ±10% disturbance of the best fitting *h*, are presented. The results indicate that the fitting has a relatively high sensitivity to *h*.

Fig. 10 shows the variation of the *h* value with Cr interlayer thickness for the Cu/Cr/diamond samples. The predicted *h* values were calculated by Eq. (3). Table 3 lists the measurement and calculation of *h* values for clarity. The experimental data differ significantly with the Cr interlayer thickness. The *h* value of the Cu/diamond interface without Cr interlay-

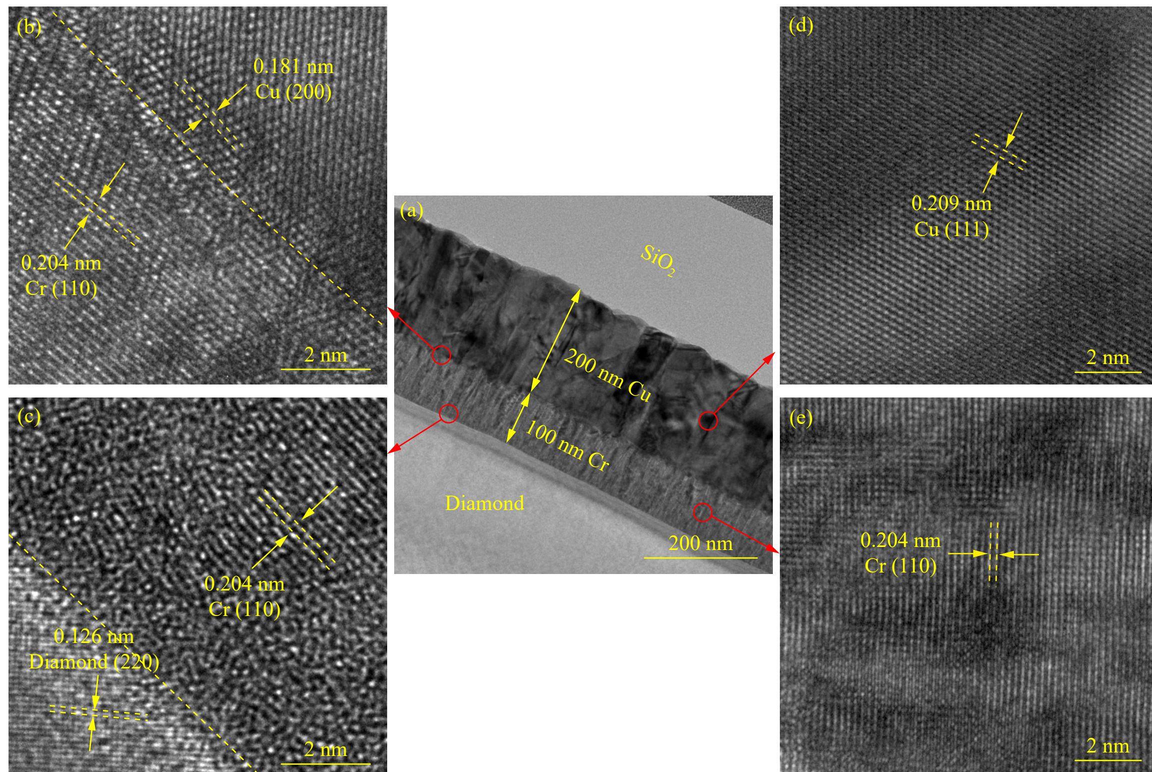

Fig. 7. TEM analysis of the Cu/Cr/diamond with 100 nm Cr: (a) STEM bright-field image of cross section of the Cu/Cr/diamond; HRTEM images of (b) Cu/Cr interface, (c) Cr/diamond interface, (d) Cu layer, and (e) Cr interlayer. The SiO_2 is coated as a protection layer during FIB milling.

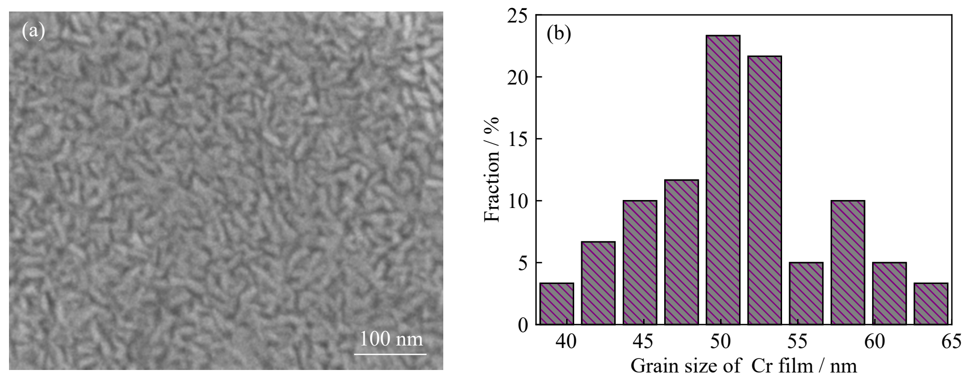

Fig. 8. SEM analysis of the 100-nm Cr film deposited on the diamond substrate: (a) surface morphology of the Cr film; (b) length distribution of the oval-shaped Cr grains.

er is measured to be 57 (+1.8, −1.9) $MW \cdot m^{-2} \cdot K^{-1}$. After inserting a Cr interlayer, the h value firstly increases to 270 (+31.1, −33.7) $MW \cdot m^{-2} \cdot K^{-1}$ at 5 nm Cr interlayer, and then gradually decreases to 63 (+2.4, −2.8) $MW \cdot m^{-2} \cdot K^{-1}$ when the Cr interlayer thickness increases to 150 nm. On one hand, the increase is mainly because the interfacial bonding at Cu/diamond interface is enhanced and the acoustic impedance mismatch between Cu and diamond is relieved by introducing a Cr interlayer. The thermal resistance associated with phonon transmission across the metal/nonmetal interface is thus reduced. The interfacial bonding strength is much higher than 100 $mJ \cdot m^{-2}$ as the sputtering metal target particles with high energy of 15–50 eV bombard the diamond substrate and deposit on the surface during magnetron sputtering [12,84]. In this regard, we argue that the acoustic impedance mismatch relief makes larger contribution to the increase of the h value than the interfacial bonding enhancement [12,84]. On the other hand, the intrinsic thermal resistance of the Cr interlayer changes with its thickness. The decrease in h value with increasing Cr interlayer thickness is conceptually intuitive since a thicker Cr interlayer would have greater intrinsic thermal resistance. Jeong *et al.* [23] and Blank and Weber [27] indicated that the h value for Au/Cu/sapphire interface with a thin Cu interlayer (1.5–30 nm) increases with increasing interlayer thickness and then tends to be steady once the interlayer thickness exceeds 5 or 10 nm. In this study, we show that the h value of Cu/Cr/diamond decreases continually with increasing the interlayer thickness from 5 to 150 nm. We note that the relatively thin interlayers are used in the literature, i.e., 7 nm Cu interlayer in Jeong *et al.*'s research [23] and 30 nm Cu interlayer in Blank *et al.*'s research [27]. Furthermore, they do not consider the scattering effect in the

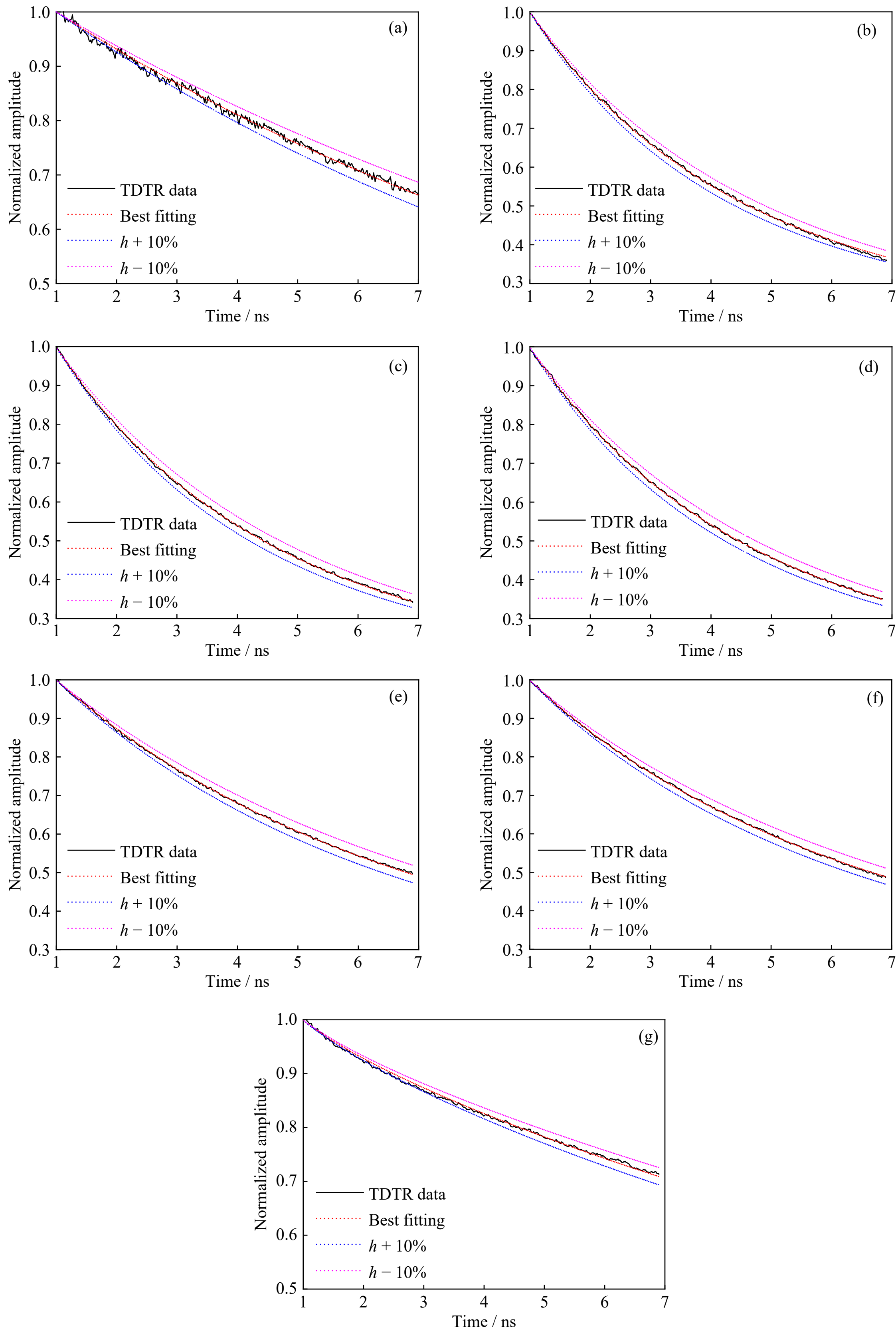

Fig. 9. TDTR data and best fitting curves as well as fitting curves with ±10% disturbance of the best fitting *h* for the Cu/Cr/diamond samples: (a) without Cr; with Cr interlayers of (b) 5 nm, (c) 10 nm, (d) 20 nm, (e) 50 nm, (f) 100 nm, and (g) 150 nm.

metal interlayer, which will be discussed later.

As shown in Fig. 10, a large deviation appears as the Cr interlayer is thicker than 20 nm. To understand the physical mechanism behind the phenomenon, the thermal conduction across the Cr interlayer is discussed in more detail. We assume in the Cr interlayer that the phononic thermal conduction pathway experiences a thermal resistance $R_p = l/\lambda_p$, which is in parallel with the thermal resistance of the elec-

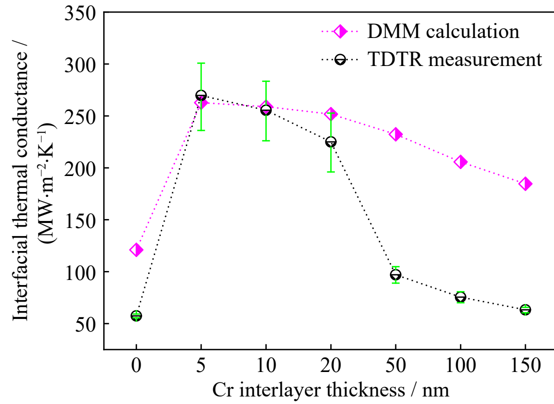

Fig. 10. Experimentally measured and theoretically predicted interfacial thermal conductance between Cu and diamond as a function of Cr interlayer thickness for the Cu/Cr/diamond samples.

Table 3. Interfacial thermal conductance calculated by DMM and measured by TDTR

Sample	l_{Cr} / nm	h / $(MW \cdot m^{-2} \cdot K^{-1})$ Calculated	Measured
Cu/diamond	—	120	57 (+1.8, −1.9)
Cu/Cr/diamond	5	263	270 (+31.1, −33.7)
	10	259	255 (+27.9, −29.4)
	20	252	225 (+27.7, −28.9)
	50	232	97 (+7.9, −8.0)
	100	206	76 (+5.1, −5.4)
	150	185	63 (+2.4, −2.8)

tronic pathway $R_e = 2\left(\frac{\lambda_e}{\lambda_e+\lambda_p}\right)^{\frac{3}{2}}\left(\frac{1}{G_{ep}\lambda_p}\right)^{\frac{1}{2}} + \frac{l}{\lambda_e}$, with l being film thickness, as shown in Fig. 11(a). The variations of thermal resistance associated with phonons and electrons in the Cr interlayer with thickness are plotted in Fig. 11(b). A critical interlayer thickness (l_{trans}) is deduced for the transition of heat carrier from electron to phonon [85]:

$$l_{trans} = \frac{2\lambda_e\lambda_p}{(G\lambda_p)^{1/2}(\lambda_e-\lambda_p)}\left(\frac{\lambda_e}{\lambda_e+\lambda_p}\right)^{\frac{3}{2}} \tag{11}$$

where the λ_e can be estimated based on the Wiedemann-Franz law of $\lambda_e = LT\sigma$, in which L is the Lorenz number and σ is the electrical conductivity of the metal [33,40]. The λ_p is estimated by $\lambda_p = \lambda - \lambda_e$ [86]. As shown in Fig. 11(b), we obtain a critical interlayer thickness of 21 nm.

The Cr interlayer thickness considerably influences which heat carrier plays a dominant role in the thermal conduction process. The phonon mean free path Λ_p of Cr is obtained to be 35.8 nm from the formula of $\lambda_p = C_p v_p \Lambda_p$ [33,37,87–88], where C_p and v_p are the phonon volumetric heat capacity and phonon velocity, respectively. When the Cr interlayer thickness is less than the critical thickness of 21 nm, the Cr interlayer thickness is also less than the phonon mean free path of 35.8 nm. The phononic thermal conduction pathway dominates, as shown in Fig. 11(b). Besides that, literature suggests that ballistic transport becomes increasingly important at length scales smaller than the mean free path for the energy carriers in a material [89]. The ballistic phonon motion in the Cr interlayer can enhance the nanoscale thermal conduction because the scattering between interfaces and phonons will be minimized. The electron mean free path Λ_e of Cr is 15.2 nm. When the Cr interlayer thickness is larger than 21 nm, the electronic thermal conduction pathway starts to dominate, as shown in Fig. 11(b). However, the Cr interlayer thickness is larger than the electron mean free path at this moment. The emitted electrons suffer from the scattering of interfaces and the nanoscale thermal conduction is lowered. In addition, when the interlayer thickness is larger than both electron and phonon mean free paths, the grain boundary effect may need to be taken into account. Take 100 nm-thick Cr interlayer for example, both electrons and phonons suffer from the scattering of interfaces and grain boundaries. Phonon and electron scattering with these structural defects results in reduced mean free paths and decreased thermal conductivity of Cr interlayer accordingly, but the electron scattering is more remarkable [90]. This explains why the three data points from 5 to 20 nm are close to and the other three data points from 50 to 150 nm are far from the theoretical predictions.

We observe in Fig. 10, however, that the experimental

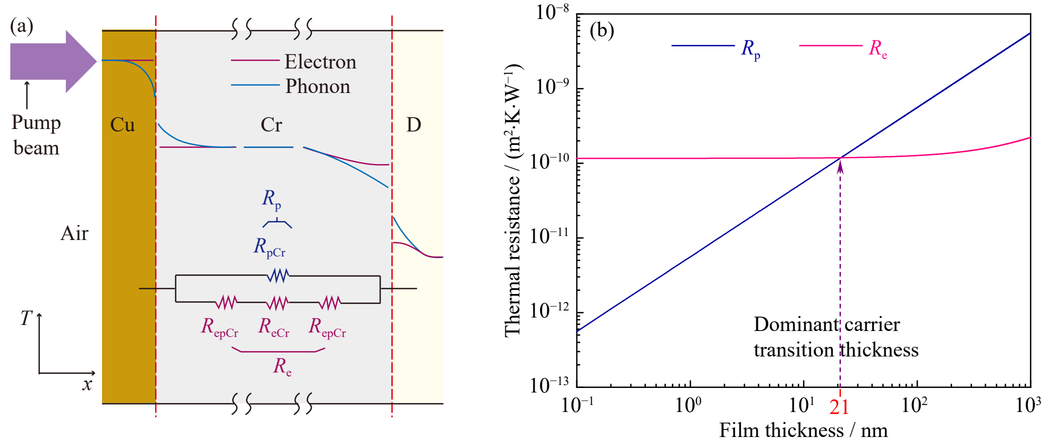

Fig. 11. (a) Thermal resistance model in the Cr interlayer and (b) variation of the thermal resistances coming from electronic and phononic pathways with Cr interlayer thickness. R_{pCr} and R_{eCr} are the phononic and electronic thermal resistances of Cr interlayer, respectively.

value for the Cu/5 nm Cr/diamond sample exceeds the DMM prediction. This suggests that it is inadequate just considering phononic thermal conduction pathway and neglecting electronic thermal conduction pathway. Here we employ the TTM and extended DMM to include the electronic thermal conduction pathway. The overall interfacial thermal resistance between Cu and diamond is obtained by Eq. (10). The calculation shows that the thermal resistance related to electronic thermal conduction pathway makes up 16.5% of the overall thermal resistance for the Cu/5 nm Cr/diamond sample. It suggests that the electronic thermal conduction pathway could not be ignored as the Cr interlayer is thinner than the electron mean free path. The experimental value for the Cu/diamond interface without Cr interlayer deviates from the prediction. The discrepancy could result from the difference between the atomic perfect interface in the prediction and the actual interface in the measurement.

4. Conclusions

The impact of Cr interlayer thickness on h of the Cu/Cr/diamond nanostructure was studied by the TDTR method. The influence of Cr interlayer thickness on h was further evaluated by comparing the experimental data with the DMM predictions. The study is very important to efficient interface engineering by tuning the Cr interlayer thickness between Cu and diamond.

(1) A valid approach to enhance h across the Cu/diamond interface is the introduction of a Cr interlayer that enhances the interfacial bonding and relieves the acoustic impedance mismatch between Cu and diamond. By gradually changing the Cr interlayer thickness from 150 to 5 nm, the h is improved by 11%–374% compared with the unmodified Cu/diamond interface. With a 5 nm-thick Cr interlayer, the h value is dramatically increased to 270 $MW \cdot m^{-2} \cdot K^{-1}$.

(2) The Cr interlayer can significantly affect the h as the dominant heat carrier shifts from electron to phonon with decreasing the Cr interlayer thickness. Efficient heat dissipation between metallic Cu and nonmetallic diamond can be achieved by phononic thermal conduction by decreasing the Cr interlayer thickness below a critical thickness of 21 nm.

(3) While the phononic thermal conduction pathway is crucial to the heat dissipation across the Cu/Cr/diamond interface, the electronic thermal conduction pathway could not be ignored as the Cr interlayer thickness is less than the electron mean free path.

Acknowledgements

This work was financially supported by the National Natural Science Foundation of China (Nos. 51871014, 51571015) and the National Youth Science Foundation, China (No. 51606193). Moon J. Kim was supported in part by the Louis Beecherl, Jr. Endowment Funds.

Conflict of Interest

The authors declare no conflict of interest.

References

[1] Y.T. Li, Y. Tian, M.X. Sun, T. Tu, Z.Y. Ju, G.Y. Gou, Y.F. Zhao, Z.Y. Yan, F. Wu, D. Xie, H. Tian, Y. Yang, and T.L. Ren, Graphene-based devices for thermal energy conversion and utilization, *Adv. Funct. Mater.*, 30(2020), No. 8, art. No. 1903888.

[2] C.G. Qiu, Z.Y. Zhang, M.M. Xiao, Y.J. Yang, D.L. Zhong, and L.M. Peng, Scaling carbon nanotube complementary transistors to 5-nm gate lengths, *Science*, 355(2017), No. 6322, p. 271.

[3] O. Yenigun and M. Barisik, Effect of nano-film thickness on thermal resistance at water/silicon interface, *Int. J. Heat Mass Transfer*, 134(2019), p. 634.

[4] Q. Zhang, X.F. Wang, S.H. Shen, Q. Lu, X.Z. Liu, H.Y. Li, J.Y. Zheng, C.P. Yu, X.Y. Zhong, L. Gu, T.L. Ren, and L.Y. Jiao, Simultaneous synthesis and integration of two-dimensional electronic components, *Nat. Electron.*, 2(2019), No. 4, p. 164.

[5] A. Hanif, Y.C. Yu, D. DeVoto, and F. Khan, A comprehensive review toward the state-of-the-art in failure and lifetime predictions of power electronic devices, *IEEE Trans. Power Electron.*, 34(2019), No. 5, p. 4729.

[6] P.P. Wang, G.Q. Chen, W.J. Li, H. Li, B.Y. Ju, M. Hussain, W.S. Yang, and G.H. Wu, Microstructural evolution and thermal conductivity of diamond/Al composites during thermal cycling, *Int. J. Miner. Metall. Mater.*, 28(2021), No. 11, p. 1821.

[7] T. Lan, Y.H. Jiang, X.J. Zhang, F. Cao, and S.H. Liang, Competitive precipitation behavior of hybrid reinforcements in copper matrix composites fabricated by powder metallurgy, *Int. J. Miner. Metall. Mater.*, 28(2021), No. 6, p. 1090.

[8] K.X. Gu, M.J. Pang, and Y.Z. Zhan, Insight into interfacial structure and bonding nature of diamond(001)/Cr_3C_2(001) interface, *J. Alloys Compd.*, 770(2019), p. 82.

[9] Ł. Ciupiński, M.J. Kruszewski, J. Grzonka, M. Chmielewski, R. Zielińsk, D. Moszczyńska, and A. Michalski, Design of interfacial Cr_3C_2 carbide layer via optimization of sintering parameters used to fabricate copper/diamond composites for thermal management applications, *Mater. Des.*, 120(2017), p. 170.

[10] Y.P. Wu, Y.N. Sun, J.B. Luo, P. Cheng, Y. Wang, H. Wang, and G.F. Ding, Microstructure of Cu-diamond composites with near-perfect interfaces prepared via electroplating and its thermal properties, *Mater. Charact.*, 150(2019), p. 199.

[11] X.Y. Liu, F.Y. Sun, L.H. Wang, Z.X. Wu, X.T. Wang, J.G. Wang, M.J. Kim, and H.L. Zhang, The role of Cr interlayer in determining interfacial thermal conductance between Cu and diamond, *Appl. Surf. Sci.*, 515(2020), art. No. 146046.

[12] G. Chang, F.Y. Sun, J.L. Duan, Z.F. Che, X.T. Wang, J.G. Wang, M.J. Kim, and H.L. Zhang, Effect of Ti interlayer on interfacial thermal conductance between Cu and diamond, *Acta Mater.*, 160(2018), p. 235.

[13] J.W. Li, H.L. Zhang, Y. Zhang, Z.F. Che, and X.T. Wang, Microstructure and thermal conductivity of Cu/diamond composites with Ti-coated diamond particles produced by gas pressure infiltration, *J. Alloys Compd.*, 647(2015), p. 941.

[14] Y. Zhang, H.L. Zhang, J.H. Wu, and X.T. Wang, Enhanced thermal conductivity in copper matrix composites reinforced with titanium-coated diamond particles, *Scripta Mater.*, 65(2011), No. 12, p. 1097.

[15] L. Lei, Y. Su, L. Bolzoni, and F. Yang, Evaluation on the interface characteristics, thermal conductivity, and annealing effect of a hot-forged Cu–Ti/diamond composite, *J. Mater. Sci. Technol.*, 49(2020), p. 7.

[16] C. Azina, I. Cornu, J.F. Silvain, Y.F. Lu, and J.L. Battaglia, Effect of titanium and zirconium carbide interphases on the thermal conductivity and interfacial heat transfers in copper/diamond composite materials, *AIP Adv.*, 9(2019), No. 5, art. No. 055315.

[17] J.W. Li, X.T. Wang, Y. Qiao, Y. Zhang, Z.B. He, and H.L.

Zhang, High thermal conductivity through interfacial layer optimization in diamond particles dispersed Zr-alloyed Cu matrix composites, *Scripta Mater.*, 109(2015), p. 72.
[18] R.X. Liu, G.Q. Luo, Y. Li, J. Zhang, Q. Shen, and L.M. Zhang, Microstructure and thermal properties of diamond/copper composites with Mo_2C *in situ* nano-coating, *Surf. Coat. Technol.*, 360(2019), p. 376.
[19] S.D. Ma, N.Q. Zhao, C.S. Shi, E.Z. Liu, C.N. He, F. He, and L.Y. Ma, Mo_2C coating on diamond: Different effects on thermal conductivity of diamond/Al and diamond/Cu composites, *Appl. Surf. Sci.*, 402(2017), p. 372.
[20] A.M. Abyzov, M.J. Kruszewski, Ł. Ciupiński, M. Mazurkiewicz, A. Michalski, and K.J. Kurzydłowski, Diamond-tungsten based coating-copper composites with high thermal conductivity produced by Pulse Plasma Sintering, *Mater. Des.*, 76(2015), p. 97.
[21] G.Z. Bai, L.H. Wang, Y.J. Zhang, X.T. Wang, J.G. Wang, M.J. Kim, and H.L. Zhang, Tailoring interface structure and enhancing thermal conductivity of Cu/diamond composites by alloying boron to the Cu matrix, *Mater. Charact.*, 152(2019), p. 265.
[22] S.W. Hung, S.Q. Hu, and J. Shiomi, Spectral control of thermal boundary conductance between copper and carbon crystals by self-assembled monolayers, *ACS Appl. Electron. Mater.*, 1(2019), No. 12, p. 2594.
[23] M. Jeong, J.P. Freedman, H.J. Liang, C.M. Chow, V.M. Sokalski, J.A. Bain, and J.A. Malen, Enhancement of thermal conductance at metal-dielectric interfaces using subnanometer metal adhesion layers, *Phys. Rev. Appl.*, 5(2016), No. 1, art. No. 014009.
[24] L.H. Wang, J.W. Li, Z.F. Che, X.T. Wang, H.L. Zhang, J.G. Wang, and M.J. Kim, Combining Cr pre-coating and Cr alloying to improve the thermal conductivity of diamond particles reinforced Cu matrix composites, *J. Alloys Compd.*, 749(2018), p. 1098.
[25] M. Blank and L. Weber, Towards a coherent database of thermal boundary conductance at metal/dielectric interfaces, *J. Appl. Phys.*, 125(2019), No. 9, art. No. 095302.
[26] R. Prasher, Acoustic mismatch model for thermal contact resistance of van der Waals contacts, *Appl. Phys. Lett.*, 94(2009), No. 4, art. No. 041905.
[27] M. Blank and L. Weber, Influence of the thickness of a nanometric copper interlayer on Au/dielectric thermal boundary conductance, *J. Appl. Phys.*, 124(2018), No. 10, art. No. 105304.
[28] S.L. Udachan, N.H. Ayachit, and L.A. Udachan, Impact of substrates on the electrical properties of thin chromium films, *Ing. Univ.*, 23(2019), No. 2.
[29] A.V. Andreyev, The wetting and bonding of diamond films by high melting point metals in the range of diamond thermodynamic stability, *Diam. Relat. Mater.*, 3(1994), No. 10, p. 1262.
[30] T. Tanaka, N. Ikawa, and H. Tsuwa, Affinity of diamond for metals, *CIRP Ann.*, 30(1981), No. 1, p. 241.
[31] R. Cheaito, J.T. Gaskins, M.E. Caplan, B.F. Donovan, B.M. Foley, A. Giri, J.C. Duda, C.J. Szwejkowski, C. Constantin, H.J. Brown-Shaklee, J.F. Ihlefeld, and P.E. Hopkins, Thermal boundary conductance accumulation and interfacial phonon transmission: Measurements and theory, *Phys. Rev. B*, 91(2015), No. 3, art. No. 035432.
[32] S. Sadasivam, N. Ye, J.P. Feser, J. Charles, K. Miao, T. Kubis, and T.S. Fisher, Thermal transport across metal silicide-silicon interfaces: First-principles calculations and Green's function transport simulations, *Phys. Rev. B*, 95(2017), No. 8, art. No. 085310.
[33] Y. Wang, Z.X. Lu, A.K. Roy, and X.L. Ruan, Effect of interlayer on interfacial thermal transport and hot electron cooling in metal-dielectric systems: An electron–phonon coupling perspective, *J. Appl. Phys.*, 119(2016), No. 6, art. No. 065103.
[34] Y. Wang, X.L. Ruan, and A.K. Roy, Two-temperature nonequilibrium molecular dynamics simulation of thermal transport across metal-nonmetal interfaces, *Phys. Rev. B*, 85(2012), No. 20, art. No. 205311.
[35] L. Chen, S.T. Chen, and Y. Hou, Understanding the thermal conductivity of diamond/copper composites by first-principles calculations, *Carbon*, 148(2019), p. 249.
[36] X.B. Li and R.G. Yang, Effect of lattice mismatch on phonon transmission and interface thermal conductance across dissimilar material interfaces, *Phys. Rev. B*, 86(2012), No. 5, art. No. 054305.
[37] S. Merabia and K. Termentzidis, Thermal conductance at the interface between crystals using equilibrium and nonequilibrium molecular dynamics, *Phys. Rev. B*, 86(2012), No. 9, art. No. 094303.
[38] K. Chu, C.C. Jia, X.B. Liang, H. Chen, W.J. Gao, and H. Guo, Modeling the thermal conductivity of diamond reinforced aluminium matrix composites with inhomogeneous interfacial conductance, *Mater. Des.*, 30(2009), No. 10, p. 4311.
[39] W. Zhang, T.S. Fisher, and N. Mingo, The atomistic Green's function method: An efficient simulation approach for nanoscale phonon transport, *Numer. Heat Transfer Part B*, 51(2007), No. 4, p. 333.
[40] B.C. Gundrum, D.G. Cahill, and R.S. Averback, Thermal conductance of metal–metal interfaces, *Phys. Rev. B*, 72(2005), No. 24, art. No. 245426.
[41] M. Blank, G. Schneider, J. Ordonez-Miranda, and L. Weber, Role of the electron–phonon coupling on the thermal boundary conductance of metal/diamond interfaces with nanometric interlayers, *J. Appl. Phys.*, 126(2019), No. 16, art. No. 165302.
[42] P.E. Hopkins, J.L. Kassebaum, and P.M. Norris, Effects of electron scattering at metal-nonmetal interfaces on electron-phonon equilibration in gold films, *J. Appl. Phys.*, 105(2009), No. 2, art. No. 023710.
[43] D.G. Cahill, W.K. Ford, K.E. Goodson, G.D. Mahan, A. Majumdar, H.J. Maris, R. Merlin, and S.R. Phillpot, Nanoscale thermal transport, *J. Appl. Phys.*, 93(2003), No. 2, p. 793.
[44] Z.B. Lin, L.V. Zhigilei, and V. Celli, Electron–phonon coupling and electron heat capacity of metals under conditions of strong electron-phonon nonequilibrium, *Phys. Rev. B*, 77(2008), No. 7, art. No. 075133.
[45] L. Guo, S.L. Hodson, T.S. Fisher, and X.F. Xu, Heat transfer across metal-dielectric interfaces during ultrafast-laser heating, *J. Heat Transfer*, 134(2012), No. 4, art. No. 042402.
[46] P.E. Hopkins and P.M. Norris, Substrate influence in electron–phonon coupling measurements in thin Au films, *Appl. Surf. Sci.*, 253(2007), No. 15, p. 6289.
[47] J.B. Liang, S. Masuya, M. Kasu, and N. Shigekawa, Realization of direct bonding of single crystal diamond and Si substrates, *Appl. Phys. Lett.*, 110(2017), No. 11, art. No. 111603.
[48] M. Lv, B. Xu, L.C. Cai, X.F. Guo, and X.D. Yuan, Auger electron spectroscopy analysis for growth interface of cubic boron nitride single crystals synthesized under high pressure and high temperature, *Appl. Surf. Sci.*, 439(2018), p. 780.
[49] W.E.S. Unger, T. Wirth, and V.D. Hodoroaba, Auger electron spectroscopy, [in] *Characterization of Nanoparticles*, Elsevier, Amsterdam, 2020, p. 373.
[50] Z. Cheng, T.Y. Bai, J.J. Shi, T.L. Feng, Y.K. Wang, M. Mecklenburg, C. Li, K.D. Hobart, T.I. Feygelson, M.J. Tadjer, B.B. Pate, B.M. Foley, L. Yates, S.T. Pantelides, B.A. Cola, M. Goorsky, and S. Graham, Tunable thermal energy transport across diamond membranes and diamond–Si interfaces by nanoscale graphoepitaxy, *ACS Appl. Mater. Interfaces*, 11(2019), No. 20, p. 18517.
[51] L.P. Zeng, K.C. Collins, Y.J. Hu, M.N. Luckyanova, A.A. Maznev, S. Huberman, V. Chiloyan, J. Zhou, X. Huang, K.A. Nelson, and G. Chen, Measuring phonon mean free path distributions by probing quasiballistic phonon transport in grating nanostructures, *Sci. Rep.*, 5(2015), art. No. 17131.
[52] K.T. Regner, D.P. Sellan, Z.H. Su, C.H. Amon, A.J.H. McGaughey, and J.A. Malen, Broadband phonon mean free path contributions to thermal conductivity measured using fre-

quency domain thermoreflectance, *Nat. Commun.*, 4(2013), art. No. 1640.
[53] R. Anufriev, A. Ramiere, J. Maire, and M. Nomura, Heat guiding and focusing using ballistic phonon transport in phononic nanostructures, *Nat. Commun.*, 8(2017), art. No. 15505.
[54] R. Rastgarkafshgarkolaei, J.J. Zhang, C.A. Polanco, N.Q. Le, A.W. Ghosh, and P.M. Norris, Maximization of thermal conductance at interfaces via exponentially mass-graded interlayers, *Nanoscale*, 11(2019), No. 13, p. 6254.
[55] I.E. Monje, E. Louis, and J.M. Molina, Role of Al_4C_3 on the stability of the thermal conductivity of Al/diamond composites subjected to constant or oscillating temperature in a humid environment, *J. Mater. Sci.*, 51(2016), No. 17, p. 8027.
[56] C. Zhang, R.C. Wang, Z.Y. Cai, C.Q. Peng, Y. Feng, and L. Zhang, Effects of dual-layer coatings on microstructure and thermal conductivity of diamond/Cu composites prepared by vacuum hot pressing, *Surf. Coat. Technol.*, 277(2015), p. 299.
[57] M. Kida, L. Weber, C. Monachon, and A. Mortensen, Thermal conductivity and interfacial conductance of AlN particle reinforced metal matrix composites, *J. Appl. Phys.*, 109(2011), No. 6, art. No. 064907.
[58] Q.P. Kang, X.B. He, S.B. Ren, L. Zhang, M. Wu, C.Y. Guo, W. Cui, and X.H. Qu, Preparation of copper-diamond composites with chromium carbide coatings on diamond particles for heat sink applications, *Appl. Therm. Eng.*, 60(2013), No. 1-2, p. 423.
[59] A. Majumdar and P. Reddy, Role of electron–phonon coupling in thermal conductance of metal-nonmetal interfaces, *Appl. Phys. Lett.*, 84(2004), No. 23, p. 4768.
[60] T. Min, Y.M. Gao, Y.F. Li, Y. Yang, R.T. Li, and X.J. Xie, First-principles calculations study on the electronic structures, hardness and Debye temperatures of chromium carbides, *Rare Met. Mater. Eng.*, 41(2012), No. 2, p. 271.
[61] Z.Q. Tan, Z.Q. Li, D.B. Xiong, G.L. Fan, G. Ji, and D. Zhang, A predictive model for interfacial thermal conductance in surface metallized diamond aluminum matrix composites, *Mater. Des.*, 55(2014), p. 257.
[62] E.T. Swartz and R.O. Pohl, Thermal boundary resistance, *Rev. Mod. Phys.*, 61(1989), No. 3, p. 605.
[63] T.Q. Qiu and C.L. Tien, Size effects on nonequilibrium laser heating of metal films, *J. Heat Transfer*, 115(1993), No. 4, p. 842.
[64] S.S. Wellershoff, J. Hohlfeld, J. Güdde, and E. Matthias, The role of electron–phonon coupling in femtosecond laser damage of metals, *Appl. Phys. A*, 69(1999), No. 1, p. S99.
[65] T. Saito, O. Matsuda, and O.B. Wright, Picosecond acoustic phonon pulse generation in nickel and chromium, *Phys. Rev. B*, 67(2003), No. 20, art. No. 205421.
[66] J. Lombard, F. Detcheverry, and S. Merabia, Influence of the electron–phonon interfacial conductance on the thermal transport at metal/dielectric interfaces, *J. Phys.: Condens. Matter*, 27(2015), No. 1, art. No. 015007.
[67] J. Hohlfeld, S.S. Wellershoff, J. Güdde, U. Conrad, V. Jähnke, and E. Matthias, Electron and lattice dynamics following optical excitation of metals, *Chem. Phys.*, 251(2000), No. 1-3, p. 237.
[68] S.S. Wellershoff, J. Gudde, J. Hohlfeld, J.G. Muller, and E. Matthias, Role of electron–phonon coupling in femtosecond laser damage of metals, *Proc. SPIE 3343, High-Power Laser Ablation*, 3343(1998), p. 378.
[69] M. Bonn, D.N. Denzler, S. Funk, M. Wolf, S.S. Wellershoff, and J. Hohlfeld, Ultrafast electron dynamics at metal surfaces: Competition between electron–phonon coupling and hot-electron transport, *Phys. Rev. B*, 61(2000), No. 2, p. 1101.
[70] S.D. Brorson, A. Kazeroonian, J.S. Moodera, D.W. Face, T.K. Cheng, E.P. Ippen, M.S. Dresselhaus, and G. Dresselhaus, Femtosecond room-temperature measurement of the electron–phonon coupling constant γ in metallic superconductors, *Phys. Rev. Lett.*, 64(1990), No. 18, p. 2172.
[71] Y. Ezzahri and A. Shakouri, Ballistic and diffusive transport of energy and heat in metals, *Phys. Rev. B*, 79(2009), No. 18, art. No. 184303.
[72] H.E. Elsayed-Ali, T.B. Norris, M.A. Pessot, and G.A. Mourou, Time-resolved observation of electron-phonon relaxation in copper, *Phys. Rev. Lett.*, 58(1987), No. 12, p. 1212.
[73] G.L. Eesley, Generation of nonequilibrium electron and lattice temperatures in copper by picosecond laser pulses, *Phys. Rev. B*, 33(1986), No. 4, p. 2144.
[74] M. Saghebfar, M.K. Tehrani, S.M.R. Darbani, and A.E. Majd, Femtosecond pulse laser ablation of chromium: Experimental results and two-temperature model simulations, *Appl. Phys. A*, 123(2017), No. 1, art. No. 28.
[75] D. Gall, Electron mean free path in elemental metals, *J. Appl. Phys.*, 119(2016), No. 8, art. No. 085101.
[76] G.S. Kumar, G. Prasad, and R.O. Pohl, Experimental determinations of the Lorenz number, *J. Mater. Sci.*, 28(1993), No. 16, p. 4261.
[77] E. Fawcett and D. Griffiths, The Fermi surface areas of chromium, molybdenum and tungsten, *J. Phys. Chem. Solids*, 23(1962), No. 11, p. 1631.
[78] D.G. Cahill, P.V. Braun, G. Chen, D.R. Clarke, S.H. Fan, K.E. Goodson, P. Keblinski, W.P. King, G.D. Mahan, A. Majumdar, H.J. Maris, S.R. Phillpot, E. Pop, and L. Shi, Nanoscale thermal transport. II. 2003–2012, *Appl. Phys. Rev.*, 1(2014), No. 1, art. No. 011305.
[79] L. Constant, C. Speisser, and F.L. Normand, HFCVD diamond growth on Cu(111). Evidence for carbon phase transformations by *in situ* AES and XPS, *Surf. Sci.*, 387(1997), No. 1-3, p. 28.
[80] Y.F. Zhu, L. Wang, W.Q. Yao, and L.L. Cao, The interface diffusion and reaction between Cr layer and diamond particle during metallization, *Appl. Surf. Sci.*, 171(2001), No. 1-2, p. 143.
[81] Y. Mizokawa, T. Miyasato, S. Nakamura, K.M. Geib, and C.W. Wilmsen, The C KLL first-derivative X-ray photoelectron spectroscopy spectra as a fingerprint of the carbon state and the characterization of diamondlike carbon films, *J. Vac. Sci. Technol. A*, 5(1987), No. 5, p. 2809.
[82] Y.F. Zhu, W.Q. Yao, B. Zheng, and L.L. Cao, Application of AES line shape analysis for the identification of interface species during the metallization of diamond particles, *Surf. Interface Anal.*, 28(1999), No. 1, p. 254.
[83] M.A. Smith and L.L. Levenson, Final-state effects in carbon Auger spectra of transition-metal carbides, *Phys. Rev. B*, 16(1977), No. 4, p. 1365.
[84] J.A. Thornton, Substrate heating in cylindrical magnetron sputtering sources, *Thin Solid Films*, 54(1978), No. 1, p. 23.
[85] Z.J. Li, S. Tan, E. Bozorg-Grayeli, T. Kodama, M. Asheghi, G. Delgado, M. Panzer, A. Pokrovsky, D. Wack, and K.E. Goodson, Phonon dominated heat conduction normal to Mo/Si multilayers with period below 10 nm, *Nano Lett.*, 12(2012), No. 6, p. 3121.
[86] N. Stojanovic, D.H.S. Maithripala, J.M. Berg, and M. Holtz, Thermal conductivity in metallic nanostructures at high temperature: Electrons, phonons, and the Wiedemann-Franz law, *Phys. Rev. B*, 82(2010), No. 7, art. No. 075418.
[87] H.C. Chien, D.J. Yao, and C.T. Hsu, Measurement and evaluation of the interfacial thermal resistance between a metal and a dielectric, *Appl. Phys. Lett.*, 93(2008), No. 23, art. No. 231910.
[88] H. Belmabrouk, H. Rezgui, F. Nasri, M.F.B. Aissa, and A.A. Guizani, Interfacial heat transport across multilayer nanofilms in ballistic–diffusive regime, *Eur. Phys. J. Plus*, 135(2020), No. 1, art. No. 109.
[89] M.E. Siemens, Q. Li, R.G. Yang, K.A. Nelson, E.H. Anderson, M.M. Murnane, and H.C. Kapteyn, Quasi-ballistic thermal transport from nanoscale interfaces observed using ultrafast coherent soft X-ray beams, *Nat. Mater.*, 9(2010), No. 1, p. 26.
[90] F.W. Mu, Z. Cheng, J.J. Shi, S. Shin, B. Xu, J. Shiomi, S. Graham, and T. Suga, High thermal boundary conductance across bonded heterogeneous GaN–SiC interfaces, *ACS Appl. Mater. Interfaces*, 11(2019), No. 36, p. 33428.